1,6-Hexanedithiol Monolayers on Au(111): A Multitechnique Structural Study

T. Y. B. Leung,† M. C. Gerstenberg, D. J. Lavrich,‡ and G. Scoles*

Department of Chemistry, Princeton University, Princeton, New Jersey 08544

F. Schreiber

Institut für Theoretische und Angewandte Physik, Universität Stuttgart, 70550 Stuttgart, Germany, and Max-Planck-Institut für Metallforschung, Heisenbergstrasse 1, 70569 Stuttgart, Germany

G. E. Poirier

National Institute of Standards and Technology, Gaithersburg, Maryland 20899

Received May 21, 1999. In Final Form: September 8, 1999

Monolayers of 1,6-hexanedithiol [$HS(CH_2)_6SH$] deposited on Au(111) from the gas phase were characterized by scanning tunneling microscopy (STM), grazing incidence X-ray diffraction (GIXD), and low-energy atom diffraction (LEAD). Molecular resolution STM images suggest that the molecules lie prone in a striped arrangement with an inter-row spacing of 5 Å. For the films prepared at an elevated temperature, two uniaxial incommensurate phases were found by GIXD. With respect to the surface substrate net, the diffraction patterns of both phases can be described by rectangular ($p \times \sqrt{3}$) nets, where p is 4.24 ± 0.01 and 4.30 ± 0.01. These values of p correspond to spacings of 12.23 ± 0.04 and 12.40 ± 0.02 Å along the nearest-neighbor (NN) direction of the substrate, whereas the spacing along the next-nearest-neighbor direction is 5 Å in both cases. The LEAD patterns can be described by a 3×1 superlattice with respect to the mesh observed by GIXD. Lattice nonuniformity and angular broadening along the NN direction were observed by GIXD. The structure of the striped phases is consistent with the molecules being fully extended and flat on the surface with their molecular C−C−C plane parallel to the surface. Using different growth protocols, including liquid-phase deposition, the order of the striped phases was observed to change considerably; however, no evidence of nucleation of other ordered phases was found. Even if denser phases exist, the striped phases may act as effective kinetic traps preventing the transition to other denser phases. The results of both varied growth conditions and performed annealing experiments can be explained by the strong molecule/substrate interaction in the striped phases, which is a consequence of the strong, but not site-specific, interaction of both sulfur atoms with the gold surface.

I. Introduction

Self-assembled monolayers (SAMs) of thiols on gold have been intensively studied because they have shown to be promising materials for microelectronics and biotechnology and can act as a model system for studying more complex membranelike surface layers. In particular, monolayers of ω-substituted thiols of the form $HS-(CH_2)_n-X$ assembled on Au(111) (hereafter denoted as $HS-C_n-X$) have been explored for different technological applications.[1] Previous work has demonstrated that there are a number of competing interactions present in self-assembled monolayers, including strong headgroup−substrate interaction, endgroup−substrate interaction, chain−chain interaction, and endgroup−endgroup interaction.[2] It is the overall balance of these interactions that governs the structure and growth of this class of organic thin films.

The dependence of the structure on the chemical nature of the endgroup has been studied for X = OH, COOH, $CH{=}CH_2$, and CH_3. The latter three endgroups resulted in a similar structure,[2a,3a] whereas $HS-C_6-OH$ was found by STM to adopt a different structure.[4] While the interaction of the carboxylic groups is expected to be significant because of the possible dimer formation, the experimental observations for $HS-C_{15}-COOH$ suggest that the van der Waals interactions for long alkyl chains may dominate. Consistently, the impact of the olefin groups in $HS-C_n-CH{=}CH_2$ on the system was not found to be large for any chain length.[3a]

* To whom correspondence should be addressed.

† Present address: Department of Chemistry, University of Illinois at Urbana-Champaign, Urbana, IL 61801.

‡ Present address: Restek Corp., 110 Benner Circle, Bellefonte, PA 16823.

(1) Ulman, A. *An Introduction to Ultrathin Organic Films from Langmuir−Blodgett to Self-Assembly*; Academic Press: New York, 1991. (b) Whitesides, G. M.; Gorman, C. B. *The Handbook of Surface Imaging and Visualization*, Hubbard, A. T., Ed.; CRC Press: Boca Raton, FL, 1995.

(2) Li, J.; Liang, K. S.; Scoles, G.; Ulman, A. *Langmuir* **1995**, *11*, 4418. (b) Bain, C. D.; Troughton, E. B.; Tao, Y.-T.; Evall, J.; Whitesides, G. M.; Nuzzo, R. G. *J. Am. Chem. Soc.* **1989**, *111*, 321. (c) Nuzzo, R. G.; Dubois, L. H.; Allara, D. L. *J. Am. Chem. Soc.* **1990**, *112*, 558. (d) Caldwell, W. B.; Campbell, D. J.; Chen, K.; Herr, B. R.; Mirkin, C. A.; Malik, A.; Durbin, M. K.; Dutta, P.; Huang, K. G. *J. Am. Chem. Soc.* **1995**, *117*, 6071. (e) Wolf, H.; Ringsdorf, H.; Delamarche, E.; Takami, T.; Kang, H.; Michel, B.; Gerber, C.; Jaschke, M.; Butt, H.-J.; Bamberg, E. *J. Phys. Chem.* **1995**, *99*, 7102. (f) Creager, S. E.; Steiger, C. M. *Langmuir* **1995**, *11*, 1852. Dhirani, A.; Zehner, R. W.; Hsung, R. P.; Guyot-Sionnest, P.; Sita, L. R. *J. Am. Chem. Soc.* **1996**, *118*, 3319. (g) Liu, G.-Y.; Fenter, P.; Chidsey, C. E. D.; Ogletree, D. F.; Eisenberger, P.; Salmeron, M. *J. Chem. Phys.* **1994**, *101*, 4301. (h) Tao, Y.-T.; Wu, C.-C.; Eu, J.-Y.; Lin, W.-L.; Wu, K.-C.; Chen, C.-H. *Langmuir* **1997**, *13*, 4018. (i) Sabatini, E.; Cohen-Boulakia, J.; Bruening, M.; Rubinstein, I. *Langmuir* **1993**, *9*, 2974. (j) Jin, Q.; Rodriguez, J. A.; Li, C. Z.; Darici, Y.; Tao, N. J. *Surf. Sci.* **1999**, *101*, 425.

(3) Leung, T. Y. B. Ph.D. Thesis, Princeton University, Princeton, NJ, 1998. (b) Eberhardt, A. Ph.D. Thesis, Princeton University, Princeton, NJ, 1996.

(4) Poirier, G. E.; Pylant, E. D.; White, J. M. *J. Chem. Phys.* **1996**, *104*, 7325.

10.1021/la9906222 CCC: $19.00 © 2000 American Chemical Society
Published on Web 11/03/1999

Recent studies have found that throughout its growth process $HS-C_9-CH_3$ exhibits a rich variety of structures, before converging to the densely packed high-coverage equilibrium structure in which the molecules pack with their molecular axes inclined by ~30° with respect to the surface normal.[5,6] These findings reflect the complexity of thiol monolayers and the difficulty, shared with Langmuir films, of achieving structural equilibrium. Further understanding of the interplay between the different interactions can be gained through the studies of α,ω-dithiol monolayers in which the adsorbates have a thiol functional group at both ends.

Several groups have utilized dithiol monolayers to make molecular devices and multilayers. Brust et al. reported that multilayer structures of copper ions sandwiched between dithiol molecules can be formed by using 1,6-hexanedithiol.[7] Ellipsometry measurements suggested that the first monolayer of dithiols adsorbed to the gold substrate with only one of the thiol groups, resulting in concomitant layer-by-layer growth. Other examples are molecular junctions fabricated using 1,4-phenyldithiol as linkers[8] and rigid nanostructures of gold clusters utilizing 1,4-phenyldimethanethiol and 4,4′-biphenyldithiol.[9]

While previous studies have focused on the electronic and photophysical properties of the nanodevices, the structural characterization of these monolayers is incomplete. To exploit the full potential of molecular electronics devices, the structure of the monolayers used to make them needs to be known. In addition, molecular-level information on how the defects affect the quality of the devices is needed.

There are a few reports, most of them of spectroscopic nature, on the characterization of α,ω-dithiol monolayers. Using ellipsometry and X-ray photoelectron spectroscopy (XPS), Tour et al. studied solution-grown monolayers and multilayers on gold films from a series of conjugated organosulfur compounds including 1,4-phenyldithiol and 4,4′-biphenyldithiol.[10a] Because multilayer formation of conjugated α,ω-dithiols on gold was observed, it was inferred that one thiol end adsorbed to the surface while the other end projected away from it. More recently, Rieley et al. employed XPS to study monolayers of 1,8-octanedithiol on gold.[10b] The data were found to be consistent with a structure with an "upright" configuration, which was similar to that suggested by Brust et al.[7] On the basis of STM observations, Nakamura et al.[11] have reported a similar upright configuration for 1,12-dodecanedithiol and a thiophene containing α,ω-dithiol monolayers on gold. Using STM and IR spectroscopy, Kobayashi et al.[12] reported a different structure for 1,8-octanedithiol on gold in which the molecules where aligned parallel to the surface.

A recent STM study has obtained information on 1,8-octanedithiol electrochemically adsorbed on Ag(111) from aqueous solution.[13] The adsorption of octanedithiol was found to give rise to close-packed SAMs lying flat on the electrode surface. Two striped structures were suggested with either a head-to-head packing or a "zipperlike" interlocking of sulfur atoms. Both phases were observed to develop domain sizes limited by the number of initial nucleation sites. More importantly, the authors inferred that the octanedithiol molecule adsorbs with only one end attached to the surface while the other forms a silver−mercaptide complex, which is subsequently adsorbed to the surface with the release of a silver ion.

With this situation in mind, we decided to use three complementary structural techniques to study 1,6-hexanedithiol [$HS-C_6-SH$] adsorbed on Au(111). Grazing incidence X-ray diffraction (GIXD) accurately measures the dimensions, the symmetry, and the average domain size of two-dimensional periodic lattices, and it is sensitive to the in-plane structure of the adsorbates. Low-energy atom diffraction (LEAD) is less precise than GIXD but has a higher surface specificity and is especially sensitive to the corrugation of the outermost surface. Scanning tunneling microscopy (STM) is, in turn, able to study, in real time and real space, the nucleation process occurring on the surface and also to measure with somewhat larger errors the lattice parameters. In particular, STM has the capability of following the structural changes during the growth at surface defects, such as steps and dislocations.

In vacuo gas-phase deposition of 1,6-hexanedithiol results in the formation of striped phases (molecules lying down in rows and showing up as stripes in STM images). As will be discussed in detail later, all available experimental evidence strongly suggests that the structure of the striped phases is likely to be composed of fully stretched molecules with their molecular axes parallel to the substrate surface. Because the structure proposed in the present study is different from the upright one commonly assumed in the literature, different growth protocols have been attempted to determine if other denser phases could be assembled in this way. No evidence of other ordered phases was found, and the structural integrity of the striped phases obtained was found to depend strongly on the deposition protocol.

The outline of this paper is as follows. The experimental procedures are explained in section II. In section III, structural studies by STM, GIXD, and LEAD are presented, and a possible structure of the striped phases is proposed. The growth of the monolayers is investigated by GIXD, and the findings are reported in section IV. The results of a GIXD study of thermal behavior of the monolayers are presented in section V, which is followed by the conclusions in section VI.

II. Experimental Details

II.A. Sample Preparation. Au(111) single crystals were used as substrates. Substrates were cleaned by repeated cycles of argon ion sputtering and annealing. The cleanliness of the substrates was signified by the observation of the well-known $23 \times \sqrt{3}$ reconstruction.[14] 1,6-Hexanedithiol (nominal purity: 96%) was purchased and used as received. Monolayers were prepared by either the conventional liquid-phase deposition or *in vacuo* gas-

(5) Schreiber, F.; Eberhardt, A.; Leung, T. Y. B.; Schwartz, P.; Lavrich, D. J.; Wetterer, S. M.; Fenter, P.; Eisenberger, P.; Scoles, G. *Phys. Rev. B* **1998**, *57*, 12476.
(6) Gerlach, R.; Polanski, G.; Rubahn, H.-G. *Appl. Phys. A* **1997**, *65*, 375.
(7) Brust, M.; Blass, P. M.; Bard, A. J. *Langmuir* **1997**, *13*, 5602.
(8) Reed, M. A.; Zhou, C.; Muller, C. J.; Burgin, T. P.; Tour, J. M. *Science* **1997**, *278*, 252.
(9) Andres, R. P.; Bein, T.; Dorogi, M.; Feng, S.; Henderson, J. I.; Kubiak, C.; Mahoney, W.; Osifchin, R. G.; Reifenberger, R. *Science* **1996**, *272*, 1323.
(10) Tour, J. M.; Jones, L., II; Pearson, D. L.; Lamba, J. J. S.; Burgin, T. P.; Whitesides, G. M.; Allara, D. L.; Parikh, A. N.; Atre, S. V. *J. Am. Chem. Soc.* **1995**, *117*, 9529. (b) Rieley, H.; Kendall, G. K.; Zemicael, F. W.; Smith, T. L.; Yang, S. *Langmuir* **1998**, *14*, 5147.
(11) Nakamura, T.; Kondoh, H.; Matsumoto, M.; Nozoye, H. *Langmuir* **1996,** *12*, 5977.
(12) Kobayashi, K.; Umemura, J.; Horiuchi, T.; Yamada, H.; Matsushige, K. *Jpn. J. Appl. Phys.* **1998**, *37* (2), L297.
(13) Cavallini, M.; Bracali, M.; Aloisi, G.; Guidelli, R. *Langmuir* **1999**, *15*, 3003.
(14) Sandy, A. R.; Mochrie, S. G. J.; Zehner, D. M.; Huang, K. G.; Gibbs, D. *Phys. Rev. B* **1991**, *43*, 4667.

phase deposition. For the conventional protocol, a clean substrate was incubated in a millimolar ethanolic solution of dithiol for 4−16 h. Prior to installation into the apparatus, the samples were rinsed several times with solvent and dried with N_2.

For *in vacuo* gas-phase depositions, the gas manifolds connected to the thiol source were pumped out for at least 30 min in order to remove any volatile impurities. Alternatively, several freeze−pump−thaw cycles were carried out prior to deposition. The purity was checked by *in situ* mass spectrometry in the STM studies or by subsequent mass spectrometry in the GIXD and LEAD studies. Several *in vacuo* growth conditions have been tried: (i) with the substrate at room temperature and the deposition rate ranging from 0.1 to 10 L/s (1 L = 10^{-6} Torr s or 10^{-4} Pa s); (ii) with the substrate at 335 K and the impingement rate kept at ∼100 L/s; and (iii) with the deposition started while the substrate was at 413 K and continued as the substrate was cooled to 323 K. In this case the deposition rate ranged from 0.02 to 5 L/s. This growth protocol is later in the paper referred to as the "high-temperature growth" protocol.

II.B. GIXD. The GIXD experiments were carried out at the beamline X10B at the National Synchrotron Light Source. Mounted on a four-circle diffractometer, a compact vacuum chamber suitable for *in situ* studies of organic thin films ($P \sim 10^{-8}$ Torr or 10^{-6} Pa) was used for the measurements. The details of the experimental setup have been described elsewhere.[3] All of the measurements were taken at a wavelength of 1.130 Å. The resolution was set by the detector slits. For most of the in-plane diffraction measurements, $\delta q_{||}$ ranged from 0.006 to 0.01 Å^{-1} while δq_z was 0.015 Å^{-1}.

The scattering geometry used is shown in Figure 1a. The total momentum transfer **q** and the perpendicular momentum transfer $\mathbf{q}_z$ are

$$\mathbf{q} = \mathbf{k}_f - \mathbf{k}_i \text{ with } |\mathbf{q}| = 2\,|\mathbf{k}_i| \sin(2\theta/2) \qquad (1)$$

and

$$|\mathbf{q}_z| = |\mathbf{k}_i|(\sin\alpha + \sin\beta) \qquad (2)$$

where $\mathbf{k}_i$ and α are respectively the incident wavevector and angle while $\mathbf{k}_f$ and β are respectively the outgoing wavevector and angle. In addition to the lattice spacing, determined from the *position* of the Bragg peaks, the monolayer domain size (L_D) can be determined from their width. After the instrumental broadening is taken into account, L_D can be estimated from the observed width, $\Delta q_{||}$, using

$$L_D \approx 2\pi/\Delta q_{||} \qquad (3)$$

Note that if other types of broadening (e.g., inhomogeneous broadening) exist, they have to be included in the calculation of the peak width.

A rectangular coordinate system is used with unit vectors **a** and **b** with |**a**| = 4.997 Å and |**b**| = 8.66 Å. The surface normal is defined as the ⟨111⟩ direction of the face-centered-cubic structure of gold. The third unit vector **c** corresponds to the (111) Bragg point and |**c**| = 2.356 Å. The reciprocal lattice units are **a***, **b***, and **c*** where |**a***| = 1.257 Å^{-1}, |**b***| = 0.726 Å^{-1}, and |**c***| = 2.667 Å^{-1}. Diffraction peaks are indexed as (*h*, *k*, *l*) and **q** equals $h\mathbf{a}^* + k\mathbf{b}^* + l\mathbf{c}^*$. Because all of the in-plane measurements were taken at *l* = 0.1, the diffraction peaks (*h*, *k*, *l*) are abbreviated as (*h*, *k*). The crystallographic directions used in this paper are indexed according to the face-centered-cubic structure of gold.

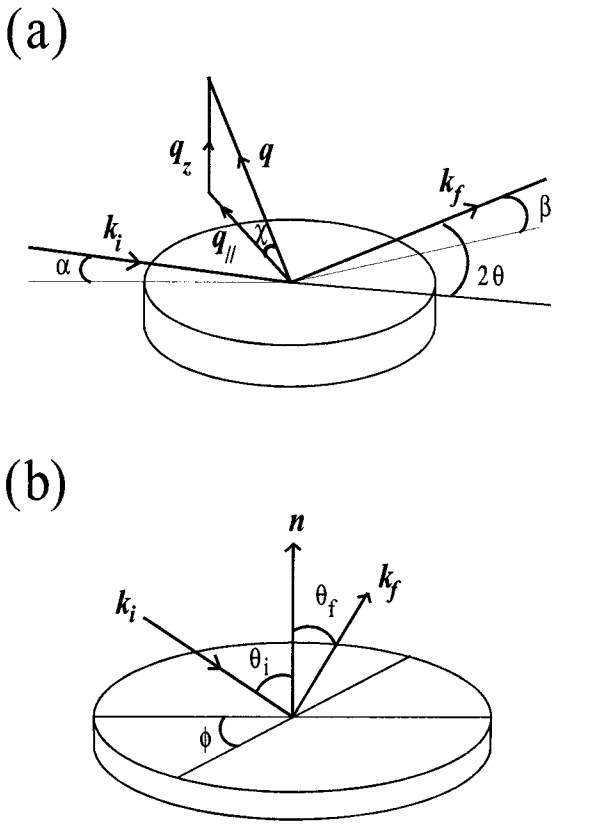

Figure 1. Schematic diagrams of the scattering geometry used (a) in the GIXD measurements and (b) in the LEAD measurements.

II.C. LEAD. The LEAD studies were performed in a bolometric detection-based atom diffractometer that allows *in situ* sample preparation. The extensive use of cryogenics provides for ultrahigh-vacuum conditions in all of the studies presented here. The diffractometer has been described in detail elsewhere.[15] The monoenergetic beam of helium (wavenumber $k_i = |\mathbf{k}_i| = 5.27$ Å^{-1} and monochromaticity $dk_i/k_i \approx 2\%$) was produced by supersonic expansion, and the incident angle θ_i was fixed at ∼60° from the surface normal. During the measurements the substrate temperature was held at 120 K. The angular distribution of the scattered helium intensity was measured by the detector for different values of θ_f. As shown in Figure 1b, an "in-plane" scattering configuration was used, i.e., the incident beam, the surface normal **n**, and the detector were all in the same plane. Thus, the parallel momentum transfer $|\mathbf{q}_{||}|$ can be determined by

$$|\mathbf{q}_{||}| = |\mathbf{k}_i|(\sin\theta_f - \sin\theta_i) \qquad (4)$$

The resolution was limited by the size of the detector. For the present studies, the $q_{||}$ resolution is ∼0.06 Å^{-1} while the azimuthal resolution is only ∼1 Å^{-1} because of the large height-to-width ratio of the slit collimating the primary beam so chosen to increase detection sensitivity.

(15) Danielson, L.; Ruiz, J. C.; Schwartz, C.; Scoles, G.; Hutson, J. M. *Faraday Discuss. Chem. Soc.* **1985**, *80*, 47. (b) Aziz, R. A.; Buck, U.; Jónsson, H.; Ruiz-Suárez, J. C.; Schmidt, B.; Scoles, G.; Slaman, M. J.; Xu, J. *J. Chem. Phys.* **1989**, *91*, 6477. (c) Rowntree, P. Ph.D. Thesis, Princeton University, Princeton, NJ, 1990. (d) Camillone, N., III. Ph.D. Thesis, Princeton University, Princeton, NJ, 1994. (e) Schwartz, P. V. Ph.D. Thesis, Princeton University, Princeton, NJ, 1998.

II.D. STM. STM studies were performed in an ultra-high-vacuum ($P \sim 10^{-10}$ Torr or 10^{-8} Pa) multichamber apparatus, which is equipped with custom-built STM and commercial XPS, quadrupole mass spectrometer probe, and a rapid-entry load-lock. The experimental design allows *in situ* preparation and chemical characterization of organic thin films. STM tips were prepared by electrochemically etching single-crystal tungsten (111) wires. All images were acquired at room temperature in a high-impedance (~10 GΩ) and constant-current (10−30 pA) mode. The systematic error in measuring the lattice spacings is ~10%.

III. Structural Studies

III.A. Lattice Dimension and Symmetry. (1) STM Results. Monolayers of *in vacuo* gas-phase grown HS−C_6−SH were characterized by STM. Figure 2a is a molecular resolution constant-current STM image of monolayers that were prepared at room temperature. The image shows rows of bright features along three symmetry-equivalent directions. The cross-sectional profiles along the rows (Figure 2b) and across the rows (Figure 2c) show that the lattice dimensions respectively are 13.3 ± 1.3 and 5.0 ± 0.5 Å. The interaxial angle[16] γ is ~95°. With respect to the substrate surface net, the overlayers can be described as a rectangular $(9 \times \sqrt{3})$ net with two molecules per unit mesh. Schematics of the unit mesh in real space and an idealized reciprocal space map are shown in parts a and b of Figure 3 , respectively. Also, the STM data shown in Figure 2a indicate that the bright features are not all aligned in the $\langle 1\bar{1}0 \rangle$ direction (i.e., the NN direction). Some features are centered along the long axis of the unit mesh (labeled by c), and some are beside the long axis (labeled by s). The implication of this "meandering" of the bright features will be discussed in section III.C.

(2) GIXD Results. Because of its high resolution and accuracy, GIXD was employed to measure the lattice spacing, the symmetry, and the interfacial structure. The monolayers were prepared following the "high-temperature growth" protocol, and the observed reciprocal space map is shown schematically in Figure 4a where the diffraction features of the monolayer and the substrate are represented by solid and open circles, respectively. Parts a and b of Figure 5 show (solid squares) the radial scans through the first-order diffraction peaks (0, 0.7) and (1, 0), respectively. The solid lines in Figure 5a,b are least-squares fits to the data assuming a linear background and a Gaussian peak shape. While the intensities will be discussed later, the peak positions are at $q_{||} = 0.507 \pm 0.001$ and 1.260 ± 0.001 Å^{-1}.

Phase coexistence was also found in the monolayers. Although the coexistence is not clearly shown in the (0, 0.7) Bragg peak, which just shifts upon annealing (solid and open squares in Figure 5a), two diffraction features are clearly present before annealing at the (0, 2.8) Bragg peak (the fourth-order peak; solid squares in Figure 5c). Upon annealing to ~423 K, an irreversible transition occurs and only one phase remains (open squares in Figure 5a,c). This phase of larger $q_{||}$ (i.e., higher density in real space) is denoted as IC1. From a least-squares fit of the data, the first-order diffraction peak along the $\langle 1\bar{1}0 \rangle$ direction of IC1 is located at 0.514 ± 0.001 Å^{-1}. The observed reciprocal space map implies that the surface net of IC1 is primitive rectangular and the unit mesh dimensions are 12.23 ± 0.04 and 4.99 ± 0.02 Å. The statistical error bars represent 3 times the standard deviations resulting from the fit to the data, while systematic errors are estimated to be on the order of 0.01

(16) Woods, E. A. *J. Appl. Phys.* **1964**, *35*, 1306.

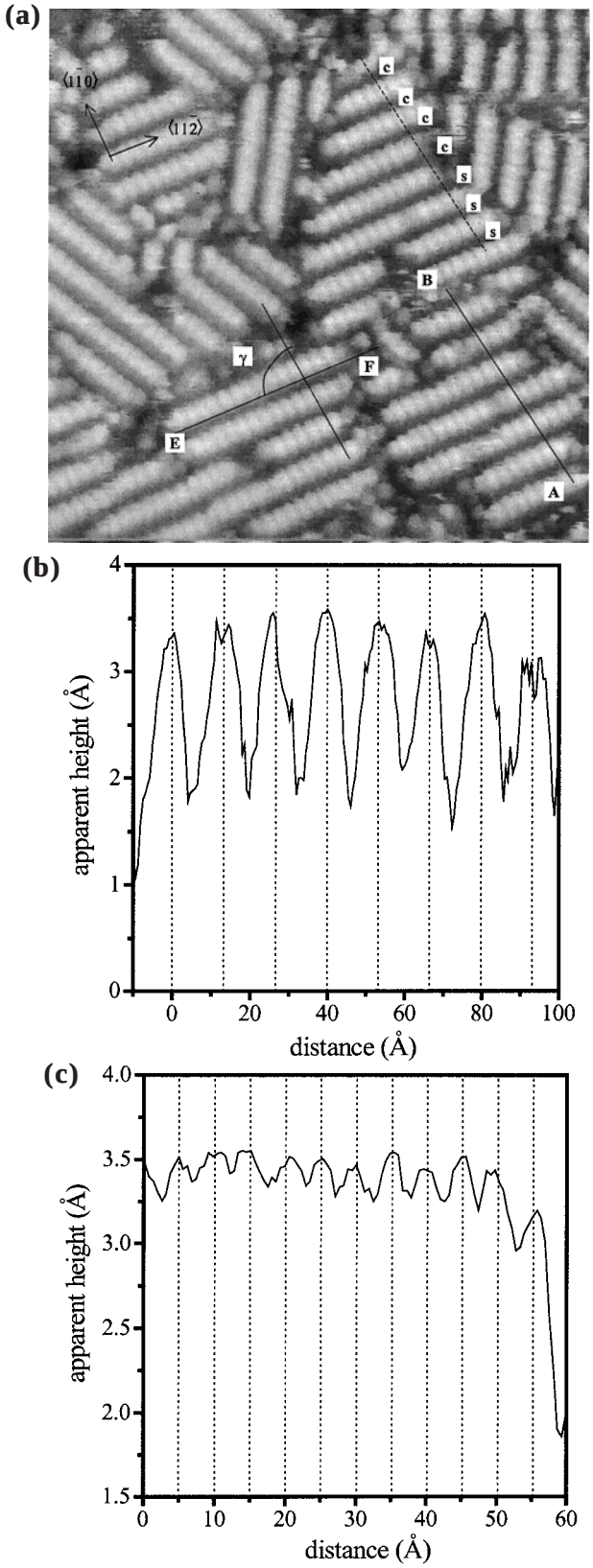

Figure 2. (a) 220 Å × 220 Å constant-current STM image showing molecular resolution of the striped phase of HS−C_6−SH prepared by in vacuo gas-phase deposition. Note that the bright features are "meandering" as explained in the text. (b) "Height" profile along the line trace AB. The dotted lines mark a spacing of 13.3 Å. (c) "Height" profile along the line trace EF. The dotted lines mark a spacing of 5.0 Å. The profiles imply a rectangular surface net with unit mesh dimensions of 13.3 ± 1.3 and 5.0 ± 0.5 Å. The meaning of the labels c and s is explained in the text.

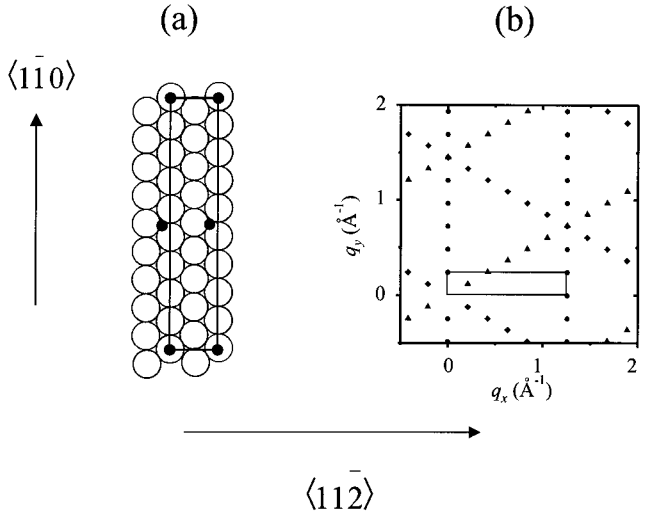

Figure 3. Schematic illustrations of the rectangular 9 × √3 surface net (part a) in real space and in reciprocal space (part b). In part a, the solid circles and open circles represent the molecules and the Au atoms, respectively. The registry of the molecules relative to the Au(111) surface and the coverage are not to be inferred from this diagram. In part b, three symmetry-equivalent domains are drawn using different symbols. The rectangles outline the unit mesh.

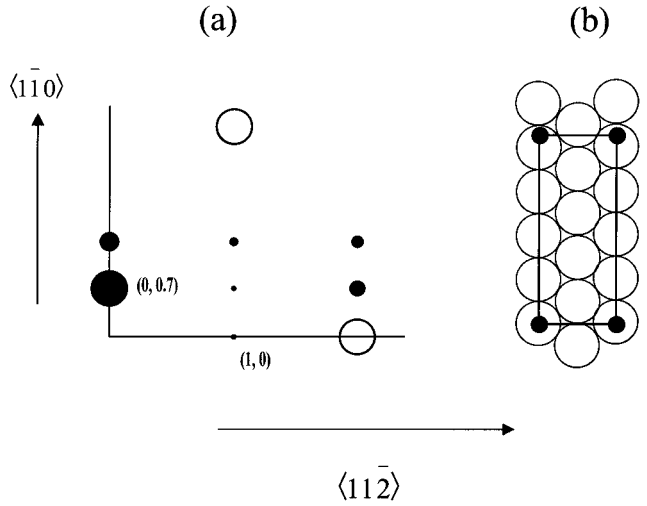

Figure 4. (a) Observed reciprocal space map for the striped phase of HS−C_6−SH (solid circles) and the Au(111) substrate (open circles) at $l = 0.1$ (i.e., $q_z = 0.2667$ Å^{-1}). The radii of the solid circles correspond to the relative intensities of the Bragg peaks. The two open circles are 60° apart. (b) Schematic illustration of the uniaxially incommensurate net in real space. Symbols are the same as those in Figure 3a. The registry of the molecules relative to the Au(111) surface and the coverage are not to be inferred from this diagram.

Å. The length 12.23 Å equals 4.24d while the length 4.99 Å is equal to $\sqrt{3}d$ where $d = 2.884$ Å is the surface lattice parameter of gold. Thus, the suggested net is uniaxially *incommensurate* with the underlying substrate and the incommensurability is along the ⟨1$\bar{1}$0⟩ direction. The real-space dimensions are illustrated in Figure 4b. The real-space long dimension of the unit mesh of the phase, which shows a peak at a smaller value of $q_{||}$(IC2), is 12.40 ± 0.02 Å or 4.30d.

Note that the characteristic lengths of the suggested surface nets are different from those inferred from the STM images but are within the experimental error of the latter. In Figure 5a,c, the arrows mark the expected peak positions for a rectangular 9 × √3 surface net. Notice that the lattice spacing of IC1 is shorter than that of IC2

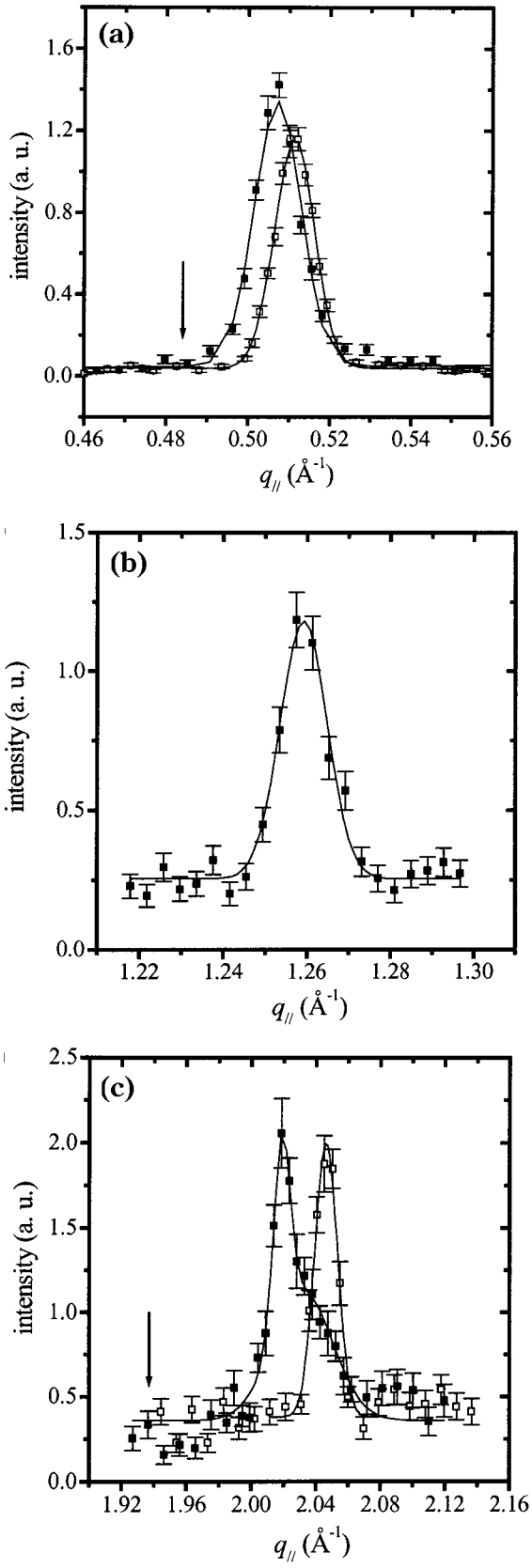

Figure 5. Radial scan GIXD data at $l = 0.1$ through (a) the (0, 0.7) peak (first order), (b) the (1, 0) peak, and (c) the (0, 2.8) peak (fourth order). The symbols (filled squares and open squares) refer to before and after annealing, respectively. The solid lines are the least-squares fits to the data. The fit to the filled squares in part c takes into account the coexistence of two phases. The arrows mark the peak positions that are expected from a commensurate rectangular 9 × √3 net.

by 1.3%, and the difference between IC1 [(4.24 × 2) × √3] and the 9 × √3 net is 5.8%.

(3) LEAD Results. The apparent discrepancy between the lattice dimensions measured by STM and GIXD motivated the LEAD study. Monolayers were prepared following the "high-temperature growth" protocol. Parts a−c of Figure 6 show diffraction patterns along the ⟨1$\bar{1}$0⟩ (NN) direction. There is a progression of diffraction peaks with a small separation in momentum transfer space. As indicated by the solid lines, most of the diffraction peaks can be explained by a periodicity of 0.169 Å^{-1}.

Figure 7 shows a diffraction spectrum along the ⟨11$\bar{2}$⟩ (NNN) direction. The positions of the more intense diffraction peaks show a periodicity of 1.257 Å^{-1} as indicated by the vertical solid lines. The spacings of 0.169 ± 0.003 and 1.257 ± 0.007 Å^{-1} correspond to a rectangular surface net with the unit mesh dimensions of 37.18 ± 0.65 and 4.995 ± 0.028 Å. Figure 8 is an idealized reciprocal space map of this net where different symbols represent the three symmetry-equivalent domains. The solid line rectangle outlines the suggested unit mesh.

Evidently, a number of peaks in the diffraction spectrum along the ⟨11$\bar{2}$⟩ direction (see Figure 7) cannot be explained by a spacing of 1.257 Å^{-1}. This can be understood by considering the instrumental resolution function, which is drawn as a dashed rectangle in Figure 8. As explained in detail elsewhere,[15d] the detector was designed to give an optimal $q_{||}$ resolution and signal-to-noise level at the cost of sacrificing the azimuthal resolution. Therefore, off-azimuthal diffraction peaks that fall in the "detection window" are also detected during the scans. The observed $q_{||}$ of these peaks is related to their true $q_{||}$ as

$$q_{||,\text{observed}} = q_{||,\text{true}} \cos \xi \qquad (5)$$

where ξ is the angle by which the peak is removed from the chosen azimuth. According to this equation, the positions of these peaks are marked as the dashed lines in the spectrum along the ⟨11$\bar{2}$⟩ direction (Figure 7). The expected off-azimuthal peak positions show an excellent agreement with the data.

The poor azimuthal resolution also explains the intensity distribution of the diffraction spectrum along the ⟨1$\bar{1}$0⟩ direction. The intensities of diffraction features around integral multiples of −1.5 Å^{-1} were found to be higher than the intensities of other diffraction peaks. By inspecting the reciprocal space map as suggested by the surface net (see Figure 8), the high intensities around these positions can be attributed to the large number of diffraction peaks which fall in the detection window. For instance, let us compare the integrated intensity around −1.5 Å^{-1} with the integrated intensity around −2.03 Å^{-1}, where only one diffraction peak contributes to the observed peak (see the arrows in the middle part of the figure). In Figure 6, the diffraction feature around $q_{||}$ of −4.3 Å^{-1} appears to be narrower than the diffraction features around $q_{||}$ of −1.5 and −2.9 Å^{-1}. This observation provides further support for the suggested surface net. Because diffraction patterns are superpositions of all of the diffraction peaks that are inside the detection window, the shapes of the diffraction features at −1.5, −2.9, and −4.3 Å^{-1} can be correlated very well with the distribution of the off-azimuthal peaks at these locations (see Figure 8).

In summary, the helium diffraction data yield a rectangular surface net with unit mesh parameters of 37.18 ± 0.65 and 4.995 ± 0.028 Å, which, within the experimental uncertainties, in one direction is *very close to 3 times* the spacing of the IC1 and IC2 phases while in

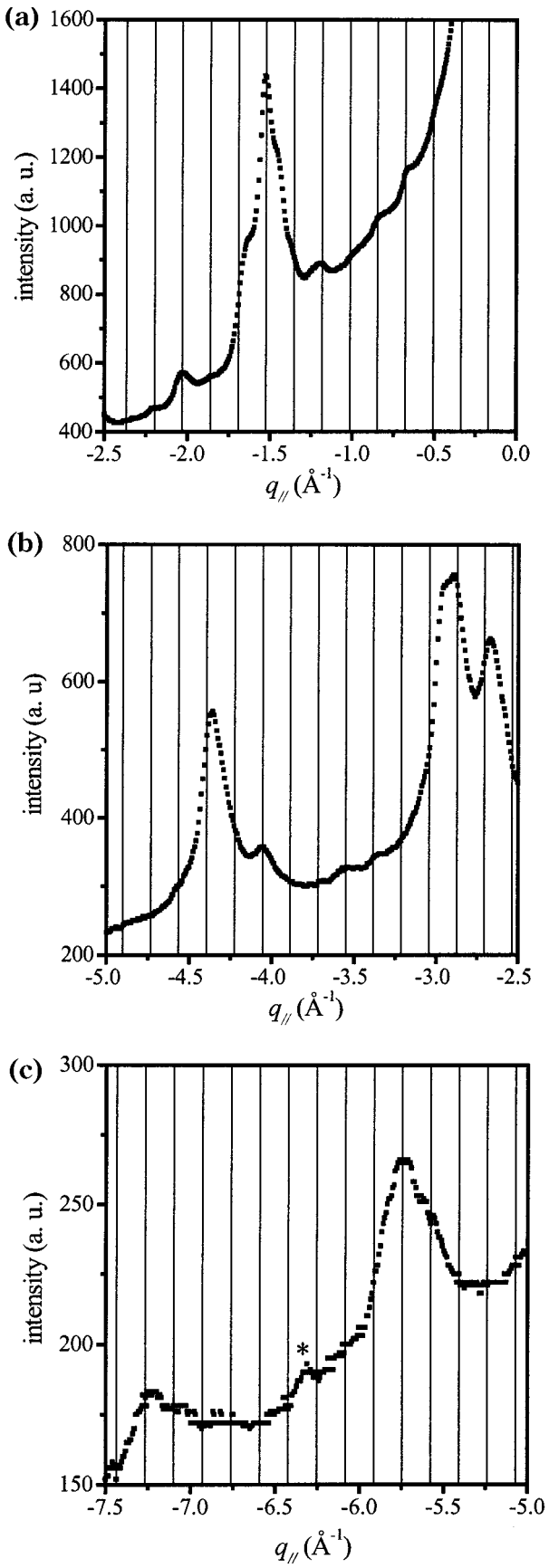

Figure 6. LEAD data taken along the ⟨1$\bar{1}$0⟩ direction. The solid lines mark a spacing of 0.169 Å^{-1}. The asterisk in part c marks a spurious peak which was not observed in all other samples.

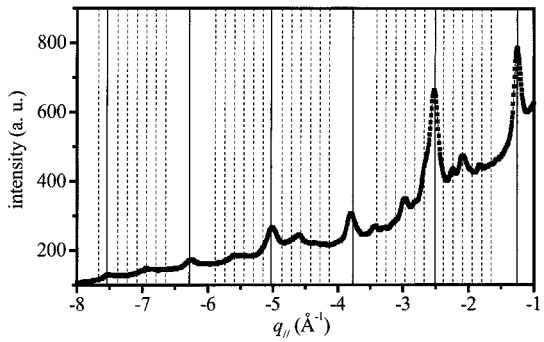

Figure 7. LEAD data taken along the $\langle 11\bar{2} \rangle$ direction. The solid lines mark a spacing of 1.257 Å^{-1}, and the dashed lines mark the expected positions of the off-azimuthal peaks, as explained in the text.

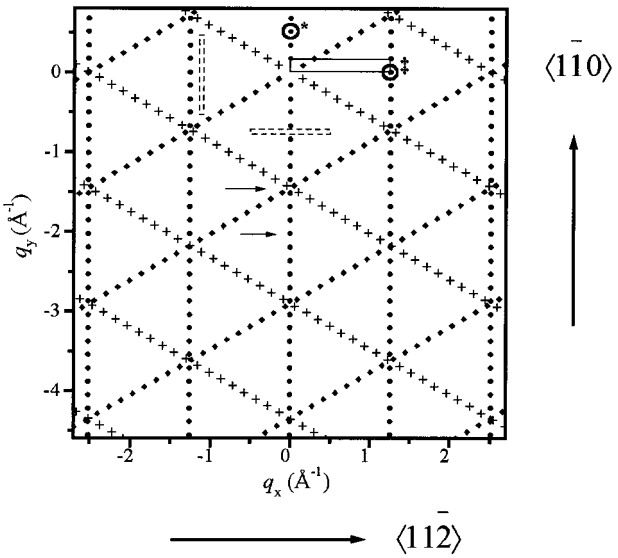

Figure 8. Representation of the reciprocal space for the incommensurate rectangular net determined by LEAD. The pattern results from the superposition of three symmetry-equivalent domains drawn with symbols (◆, ●, +). The rectangle (solid line) outlines the unit mesh. The open circles mark the peaks at 0.507 Å^{-1} (with symbol *) and at 1.257 Å^{-1} (with symbol ‡) which are also observed by GIXD. Note that the dashed-line boxes are the resolution function of the apparatus for diffraction spectra along the two main crystallographic directions. Off-azimuthal peaks can fall in the detector window as explained in the text.

the other direction coincides with $\sqrt{3}$ times the gold atomic spacing. Figure 9 is a schematic of the real-space unit mesh. A uniaxially incommensurate unit mesh was therefore measured by both diffraction probes.

Although the absence of long-range periodicity in the STM images suggests a commensurate net, the results are consistent with the diffraction results within the mutual experimental uncertainties. However, it is surprising that no Moiré patterns were observed, since they are expected for incommensurate overlayers. The reasons why the superlattice observed by atom diffraction was not observed by GIXD will be discussed later.

III.B. Peak-Width Analysis of the X-ray Data. High-resolution GIXD can reveal information on the average domain size and the presence of certain types of lattice disorder. When the radial scans through the (0, 0.7) Bragg peak and its higher order peaks are examined, the measurements show that the characteristic peak widths for the monolayers, $\Delta q_{\text{intrinsic}}$, depend on the in-plane momentum transfer, $q_{||}$, in both the IC1 and IC2 phases.

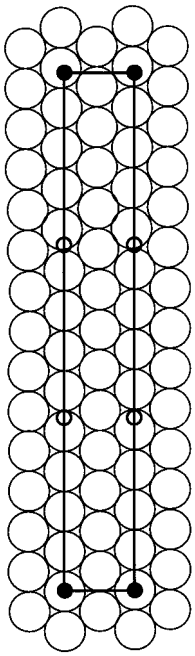

Figure 9. Real-space illustration of the incommensurate net (solid circles) suggested by LEAD spectra. Note that it can also be described as a 3 × 1 superlattice with respect to the net (small open circles) suggested by GIXD studies. The registry of the molecules relative to the Au(111) surface (large open circles) and the coverage are not to be inferred from this diagram.

The dependence implies that both phases exhibit displacement disorder along the $\langle 1\bar{1}0 \rangle$ direction.

For the analysis of the lattice disorder, the observed radial peak width, $\Delta q_{\text{total,observed}}$, is first corrected for resolution.[17,18] To a good approximation,

$$(\Delta q_{\text{total,observed}} \cos \chi)^2 = (\Delta q_{\text{resolution}} \cos \chi)^2 + \Delta q_{\text{intrinsic}}{}^2 \quad (6)$$

where $\Delta q_{\text{total,observed}}$ is the total (observed) peak width, $\Delta q_{\text{resolution}}$ is the width determined by the slit setting, and the term cos χ is a correction factor for the scattering geometry used in the experiments.[18] Besides the finite domain size, different types of lattice disorder may also contribute to $\Delta q_{\text{intrinsic}}$. According to the type of disorder, $\Delta q_{\text{intrinsic}}$ can depend in different ways on $q_{||}$.[17]

In the following we will adopt simple models described in ref 17 because a more sophisticated treatment would require an even more extended data set. On the basis of these models, we will distinguish between two types of disorder. In the first type, the lattice spacing exhibits fluctuations about the ideal spacing, with the long-range order being preserved. Then $\Delta q_{\text{intrinsic}}$ can be written as[17]

$$\Delta q_{\text{intrinsic}} = a + b_1 q_{||} \quad (7)$$

In the disorder of the second type, the spacing between two successive lattice points varies about an average value but the spacing between two given lattice points is not related to the neighboring spacing, i.e., the fluctuations are random. This leads to[17]

$$\Delta q_{\text{intrinsic}} = a + b_2 q_{||}{}^2 \quad (8)$$

(17) Guinier, A. *X-ray Diffraction*; W. H. Freeman and Company: San Francisco, 1963.
(18) Robinson, I. K. *Aust. J. Phys.* **1988**, *41*, 359.

In both cases, the term a is the width due to the finite average domain size of the monolayers.

Parts a and c of Figure 5 show the radial scans through the (0, 0.7) and (0, 2.8) peaks of the IC1 phase, respectively (see the open squares). Clearly, the fourth-order peak is wider than the first-order peak. Least-squares fits of the data with a Gaussian function and a linear background give a peak width of 0.0100 ± 0.0002 Å^{-1} for the (0, 0.7) peak and a peak width of 0.014 ± 0.001 Å^{-1} for the (0, 2.8) peak. Notice that, in the present study, the instrumental broadening $\Delta q_{\text{resolution}}$ increases with the angle χ which is $\sim$27° for the first-order peak and $\sim$7° for the fourth-order peak.[18] The $\Delta q_{\text{resolution}}$ contributions to the total width are thus 0.0099 and 0.0064 Å^{-1} for the first-order peak and the fourth-order peak, respectively. Because only two data points are available and the (0, 0.7) peak is instrument-resolution-limited, the functional form of $\Delta q_{\text{intrinsic}}$ cannot be determined. The domain size is found to be substrate-limited at $\sim$2000 Å (see below), and it implies a to be 0.003 Å^{-1} (2π/2000 Å). Assuming a linear $q_{||}$ dependence (i.e., eq 7 to be valid), the mean variation of the lattice parameter can be estimated to be more than 0.4%.

Similarly, the lattice nonuniformity in the IC2 phase was investigated. The radial widths of four peaks was measured. After accounting for the phase coexistence with IC1 and the instrumental effect, $\Delta q_{\text{intrinsic}}$, the characteristic peak width for the monolayers, were found. The $\Delta q_{\text{intrinsic}}$ values of the four diffraction peaks of IC2 are plotted as a function of $q_{||}$ (Figure 10a) and $q_{||}^2$ (Figure 10b). The lines are the least-squares fits to the data. Apparently, it is difficult to discern which model fits better, i.e., whether the disorder is of the first type or the second type. In general, one may even expect that both types of lattice disorder exist in the monolayers and the peak width will behave like:

$$\Delta q_{\text{intrinsic}} = a + b' q_{||}^2 + b'' q_{||}^2 \qquad (9)$$

While it is hard to determine the coefficients a, b', and b'' with high accuracy, the data put some constraints on the contribution of each type of disorder. From the fit to the data, the linear broadening (disorder of the first type) indicates a to be close to zero, whereas the quadratic broadening (disorder of the second type) suggests a to be 0.004 Å^{-1}. Given that the substrate has an average domain size of $\sim$2000 Å, a should be close to 0.003 Å^{-1}. Therefore, the quadratic broadening seems to be dominant, yet it is possible that both types of disorder coexist.

Finally, GIXD was also employed to examine possible orientational disorder in the monolayers. The observed azimuthal width of the diffraction peak ($\Delta q_{\text{azimuthal}}$), the width due to the instrumental resolution (Δq_{inst}), the width due to a finite domain size (a), and the width due to the angular broadening (Δq_{b}) are related by

$$\Delta q_{\text{azimuthal}}^2 = \Delta q_{\text{inst}}^2 + a^2 + \Delta q_{\text{b}}^2 \qquad (10)$$

For the present experimental configuration, $\Delta q_{\text{azimuthal}}$ is measured by an azimuthal scan through a diffraction feature. Let $d\phi$ be the width of the diffraction peak in azimuthal angle ϕ; then

$$d\phi \approx \Delta q_{\text{azimuthal}}/q_{||} \qquad (11)$$

Because Δq_{inst} is very small and a is independent of $q_{||}$, $\Delta q_{\text{azimuthal}}$ is independent of $q_{||}$ if there is no angular broadening. With $\Delta q_{\text{azimuthal}}$ constant, $d\phi$ is thus inversely proportional to $q_{||}$. Parts a and b of Figure 11 show the azimuthal scans through the (0, 0.7) peak and the fourth-order peak of the IC1 phase, respectively. The solid lines are the least-squares fits to the data (solid squares) with a linear background and a Lorentzian peak shape. The width of the (0, 0.7) peak is $0.314° \pm 0.014°$, and the width of the fourth-order peak is $0.116° \pm 0.012°$. The data clearly show that the azimuthal width of these peaks is not limited by the domain size and imply that IC1 is orientationally disordered. Notice that, from the (0, 0.7) peak width, the domain size of IC1 is derived to be $\sim$2200 Å, i.e., substrate-limited. Likewise, the IC2 phase is found to be orientationally disordered as well (data not shown).

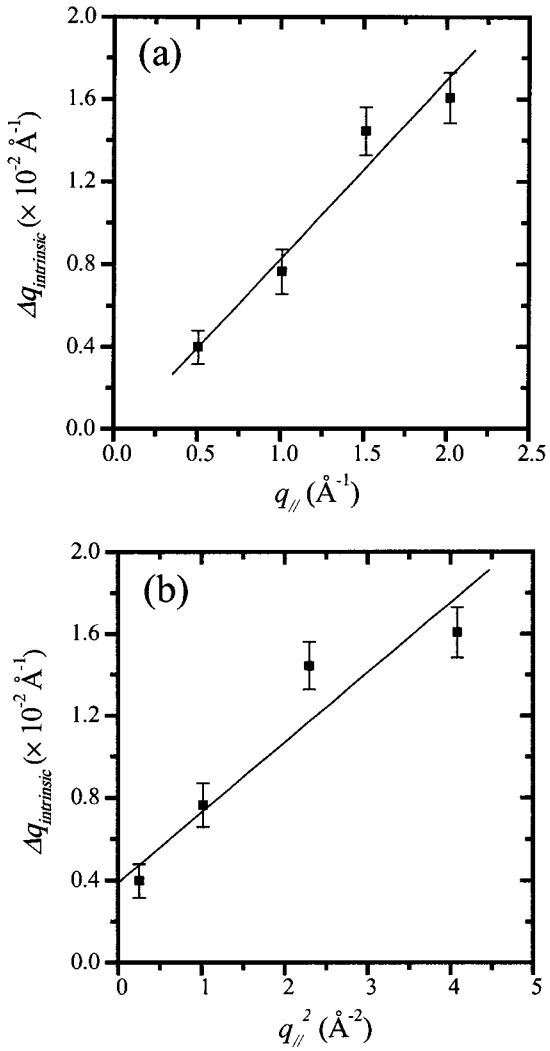

Figure 10. $\Delta q_{\text{intrinsic}}$ of the four peaks of the IC2 phase plotted as a function of (a) $q_{||}$ and (b) $q_{||}^2$. The solid lines are the least-squares fits to the data.

To conclude, the data suggest a rather complex scenario with respect to the type of disorder present in the system. While more data are needed for a more detailed analysis, the data available appear to be consistent with the STM observation of "meandering" bright features. This is most likely a consequence of the competing chemisorption of the two thiol groups on inequivalent sites of the substrate.

III.C. Proposed Structural Model for the Striped Phases. The lattice dimensions determined by STM, GIXD, and LEAD provide detailed structural information for the striped phases (IC1 and IC2). With respect to the substrate surface net, the striped phases can be described as a primitive rectangular $p \times \sqrt{3}$ net. The striped phases are similar to the striped phase of monolayers of 1,8-octanedithiol on gold observed in an earlier STM study.[12] It is quite possible that the adsorbates are lying flat on

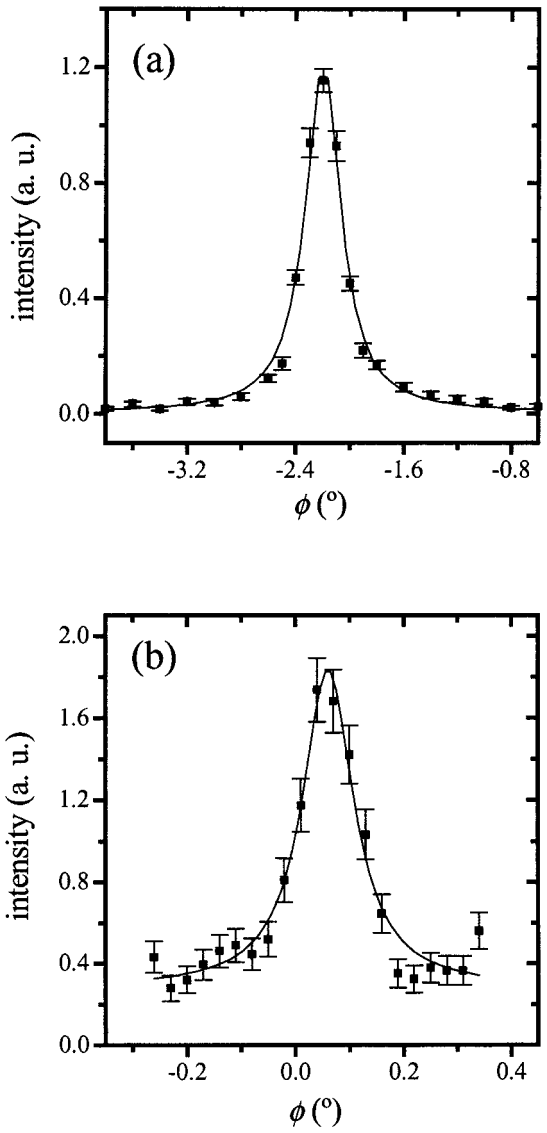

Figure 11. Data (solid squares) and the Lorentzian fits (solid lines) of the azimuthal scans through (a) the (0, 0.7) peak and (b) the (0, 2.8) peak of the IC1 phase.

the surface with the alkyl chains fully extended and the plane containing the carbon atoms parallel to the substrate. Similar packing has also been observed in the monolayers of *n*-alkanethiols on Au(111)[6,19,20] and *n*-alkanes on Pt(111).[21] While earlier work already reported that the dithiol molecules form a striped phase,[11,12] the periodicity along the $\langle 11\bar{2}\rangle$ direction (i.e., the spacing across the rows) is, for the first time, accurately measured in the present study. All of the techniques employed find the short axis of the unit mesh (along the $\langle 11\bar{2}\rangle$ direction) to be 5 Å, within experimental uncertainties, which is equal to $\sqrt{3}$ times the lattice spacing of Au(111). Notice that this is also the lattice spacing of the commensurate short periodicity of the striped phases of $HS-C_n-CH_3$,[20] which can be attributed to the packing constraints of the hydrocarbon chains and/or the corrugation of the gold substrate. Thus, the unit mesh dimensions observed for $HS-C_6-SH$ indicate that the molecules are lying flat on the surface with their alkyl chains fully extended.

The long side of the unit mesh observed by GIXD (12.40 and 12.23 Å) is close to the length of a dithiol fragment[22] suitably increased by a ~2.9 Å S−S distance. Note that while a typical S−S bond is on the order of 2 Å, the van der Waals distance between two S atoms is comprised between 3.6 and 4 Å. The molecular resolution STM image shown in Figure 2a shows that the bright features are elongated. The shape of those bright features is different from those of the striped phase of $HS-C_n-CH_3$, which were found to be round.[19,23] If the bright features are associated with sulfur atoms,[24] the elongated features observed in the striped phases of $HS-C_6-SH$ suggest that there are two sulfur atoms in close proximity of each other.

The long side of these features is parallel to the $\langle 1\bar{1}0\rangle$ direction, i.e., the NN direction of the substrate (Figure 2a). Assuming that the features are the sulfur pairs belonging to neighboring molecules, this observation suggests that the sulfur pairs align in rows parallel to the $\langle 110\rangle$ direction. However, as mentioned earlier, while following this general alignment direction, the features may slightly alter their positions perpendicularly to this direction (see features labeled c and s in the figure). Because the domain size in the monolayer at which the images were acquired is rather small, further studies are needed to clarify if this "meandering" of the sulfur pairs is intrinsic to this system or if it disappears after the films have been annealed. Note that the weak intensity of the (1,0) peak seen in X-ray diffraction may be related to the sulfur pairs' meandering and the consequent presence of partially destructive interference.

Next, it is useful to consider the information provided by the LEAD data which have shown the existence of a 3×1 superlattice of the surface net measured by GIXD. While X-rays primarily scatter from the sulfur atoms and STM tunneling takes place possibly through the sulfur atoms, helium is scattered by the corrugation of the surface potential, which is governed by a number of factors including the vertical position of the adsorbates. Two different scenarios can be invoked to explain the existence of the 3×1 superlattice detected in the atom diffraction experiments. They are (i) the existence of a height modulation of the substrate and (ii) a height modulation of the dithiol molecules which may be due to a modulation in the binding of the sulfur pairs.

As gold has a much higher electron density than sulfur and carbon, the scattered X-rays are very sensitive to even a slight modulation of the surface gold atoms. As no evidence of modulation of the surface gold atoms was detected in the GIXD experiments, height modulation of the surface gold atoms is unlikely to be present. Because the lattice nets are incommensurate, some molecular height modulation has to be expected. Recently, the formation of sulfur pairs in equilibrium monolayers of $HS-C_9-CH_3$ suggested by Fenter et al.[25] has been confirmed using standing wave X-ray photoelectron spectroscopy.[26] In that work, two different positions have been suggested for the sulfur atoms of each pair. It is

(19) Poirier, G. E.; Tarlov, M. J.; Rushmeier, H. E. *Langmuir* **1994**, *10*, 3383.
(20) Camillone, N., III; Leung, T. Y. B.; Schwartz, P.; Eisenberger, P.; Scoles, G. *Langmuir* **1996**, *12*, 2737.
(21) Firment, L. E.; Somorjai, G. A. *J. Chem. Phys.* **1977**, *66*, 2901.
(22) The C−C and C−S bond angles are 112°. The C−C bond length is 1.541 Å, and the C−S bond length is 1.81 Å. Without both of the S-bonded H atoms, the dithiol fragment is estimated to be 9.4 Å.
(23) Poirier, G. E.; Pylant, E. D. *Science* **1996**, *272*, 1145.
(24) Theoretical studies suggest that sulfur atoms should be imaged as a protrusion on metal surfaces [Lang, N. D. *Phys. Rev. Lett.* **1986**, *56*, 1164]. Also, both experimental and theoretical investigations have shown that sulfur atoms are imaged as bright features on Ni(100) surfaces [Partridge, A.; Tatlock, G. J.; Leibsle, F. M.; Flipse, C. F. J.; Hörmandinger, G.; Pendry, J. B. *Phys. Rev. B* **1993**, *48*, 8267].
(25) Fenter, P.; Eberhardt, A.; Eisenberger, P. *Science* **1994**, *266*, 1216.
(26) Fenter, P.; Schreiber, F.; Berman, L.; Scoles, G.; Eisenberger, P.; Bedzyk, M. J. *Surf. Sci.* **1998**, *412/413*, 213; **1999**, *425*, 138.

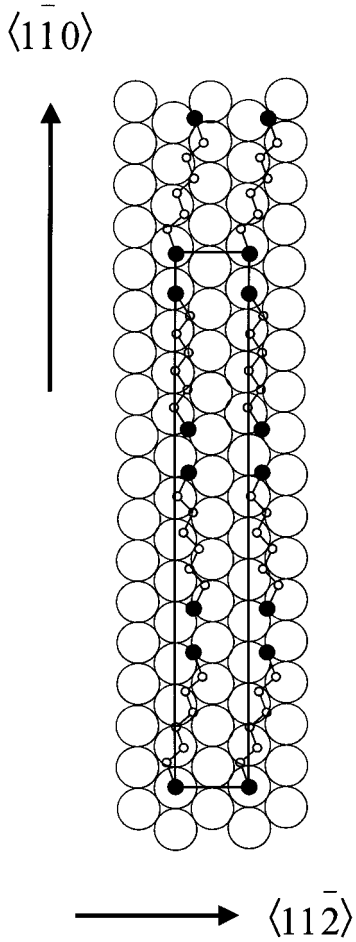

Figure 12. Proposed structure for the striped phases of HS−C_6−SH, assuming C−C and C−S bond angles of 112°, a C−C bond length of 1.541 Å, and a C−S bond length of 1.81 Å. The open circles, small open circles, and solid circles represent Au atoms, C atoms, and S atoms, respectively. The rectangle highlights the unit mesh observed by LEAD.

therefore possible that also in the HS−C_n−SH case there are multiple sulfur binding sites which are not too far from each other in energy. Because the relative position of the two sulfur endgroups is fixed by the length of the alkyl chains, it is possible that, in the direction of the chains, the atoms of the dithiol molecules find themselves every three molecules at the same height above the gold substrate so producing the 3 × 1 superlattice.

Although further studies are required to fully explain the tripling in the periodicity (for instance, a structural study of monolayers of dithiols with different chain lengths would be quite useful), the atom diffraction data suggest that the sulfur atoms are not adsorbed at any particular site.

In light of the above argument, a possible molecular structure of the striped phases of HS−C_6−SH is proposed which consists of molecules lying prone on the surface with the C−C−C molecular plane parallel to the surface of the substrate (see Figure 12). The hydrocarbon backbones are fully extended and in all-trans conformation. The distance between the molecules is 12.39 Å (37.18 Å/3), and the sulfur atoms bind on the substrate in a number of ways. The sulfur pairs from the adjacent fragments are parallel to the NN direction of the substrate, and they may "meander" around this direction. In fact, because the (1,0) diffraction peak in Figure 4 is very weak, the hydrocarbon chain connecting two S atoms and the long axis of the unit cell (the ⟨1$\bar{1}$0⟩ direction of the substrate) should not be parallel, which is consistent with the meandering effect.

IV. Growth Conditions

The structures of the monolayers grown *in vacuo* in this study disagree with previous studies,[7−10] where it is assumed that the hydrocarbon backbones in dithiol monolayers are positioned more or less vertically. In an attempt to clarify this issue, different preparation methodologies to create the "standing-up" phase have been explored. Previous studies in our laboratory and others have demonstrated that by prolonged dosing HS−C_9−CH_3 undergoes a phase transition from the striped phase, in which molecules are lying flat on the substrate, to the "standing-up" phase, in which the hydrocarbon backbones are aligned along the surface normal.[5,6] The same mechanism was also observed in monolayers of functionalized thiols, such as HS−C_6−OH.[23] *In situ* GIXD and STM studies were performed to investigate if other phases appear in HS−C_6−SH monolayers after extended dosing. Both STM and GIXD results are in good agreement (data not shown) and suggest that a prolonged dosing is not conducive to the making of other denser phases.

In previous work[3b,5,6,19,20,27] it has been shown that the self-assembly process of HS−C_{10}−CH_3 monolayers occurs by a low-density striped phase through a complex, intermediate density stage, where little long-range order is present, to the final standing up c(4 × 2) phase which grows when the coverage goes above a critical value.[28] One may then pose the question as to whether the density of domain boundaries of a particular striped phase affects the subsequent growth behavior of that layer. STM was employed to monitor if other phases nucleate for monolayers with a high density of domain boundaries by extended dosing at room temperature. No evidence of other phases was observed. The observations suggest that for the growth conditions of this experiment the density of the domain boundaries is not the limiting factor in producing kinetic traps on the road to the formation of the standing-up phase.

Another growth protocol, in which the deposition was carried out at an elevated temperature and with a very high impingement rate of dithiol, has been tried. The conjecture was that the mobility of the adsorbate increases at higher substrate temperatures allowing the monolayer to escape from possible kinetic traps and thereby succeeding in increasing the surface coverage. *In situ* GIXD studies were conducted for a monolayer which was grown at 335 K with an impingement rate of ∼100 L/s. Upon an exposure of $\sim 7 \times 10^5$ L, no evidence of ordered phases other than the incommensurate phase IC1 was observed. The results indicate that at 335 K the mobility is still too low to attain a surface coverage higher than that in the striped phase.

Traditionally, monolayers of thiols on gold have been prepared by immersing a clean gold substrate into a millimolar solution of thiol for hours at room temperature. This raises the question of whether other phases can be obtained by liquid-phase deposition. Specifically, does the solvent play a crucial role in the assembly process? To answer this question, monolayers were prepared by conventional methodology and then characterized by STM and GIXD. Figure 13 shows the STM images acquired for

(27) Schwartz, P.; Schreiber, F.; Eisenberger, P.; Scoles, G. *Surf. Sci.* **1999**, *423*, 208. (b) Yamada, R.; Uosaki, K. *Langmuir* **1997**, *13*, 5218.

(28) It should be noted, however, that beyond the initial p(11 × $\sqrt{3}$) phase other low-density phases have been seen[6] which if observed with a local probe, can be seen to play a role in the intermediate stages of the growth [Poirier, G. E. *Langmuir* **1999**, *15*, 1167].

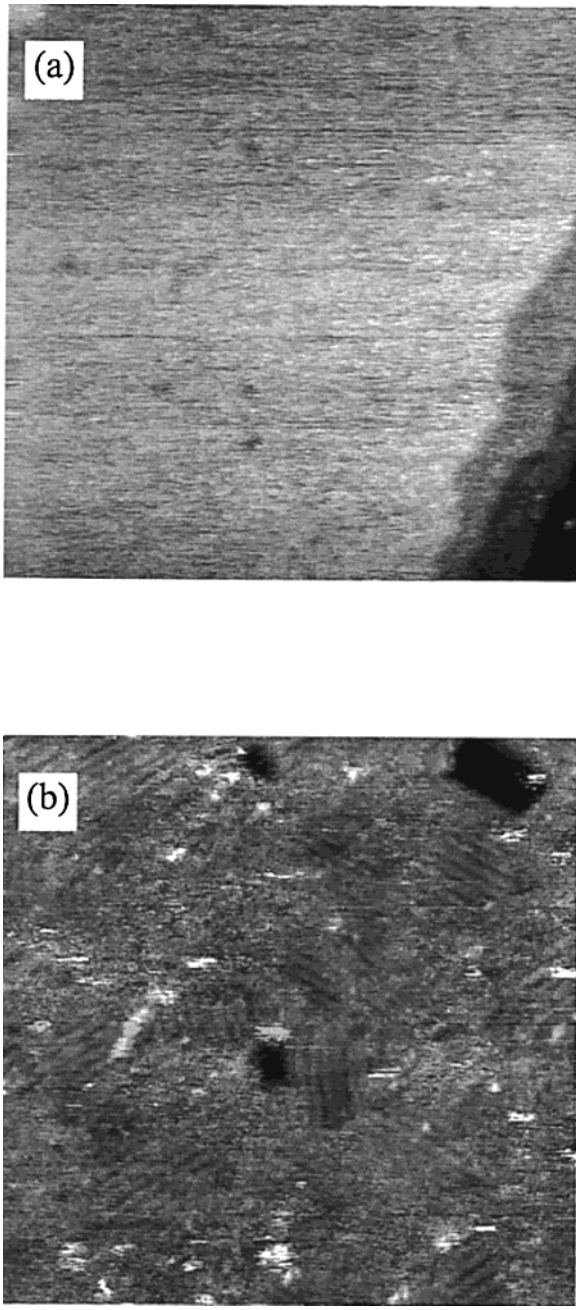

Figure 13. 500 Å × 500 Å constant-current STM images of (a) a freshly prepared solution-grown sample and (b) after annealing to 383 K the striped phase and vacancy islands.

a solution-grown sample as prepared (Figure 13a) and after annealing at 383 K (Figure 13b). No ordered phase was observed in the as-prepared sample. In the annealed sample, small domains of the striped phase and vacancy islands were observed. GIXD was also employed to determine if there were any ordered phases underneath a disordered multilayer. The GIXD results are consistent with the STM results, and no other phases were observed in the solution-grown monolayers. In other words, if other ordered phases exist, the domains are smaller than the detection limit of GIXD (i.e., significantly smaller than 50 Å in this case). Solution- and gas-phase-grown monolayers have been further characterized by XPS (data not shown). Both the sulfur 2p and carbon 1s features were found to be more prominent in the solution-grown samples, suggesting the possibility of a higher surface coverage for these species. However, because no order was found with any of the structural techniques employed, the meaning of this observation is not clear as the existence of an upright phase is not the only hypothesis that could explain the measurements. However, the observation is reported for sake of completeness and objectivity. Finally, we note that in the XPS measurements we detected no features in the region where the oxygen 1s lines normally appear, indicating the absence of sulfonate species.

The growth attempts in this study only cover a limited range of growth parameters (substrate temperature, impingement rate, with or without solvent); nevertheless, the results are very suggestive that the dithiol molecules at the very least do not readily form other denser phases. The difference in growth behavior between $HS-C_6-SH$ and $HS-C_9-CH_3$ can be rationalized by the energetics involved. In the case of the alkanethiol, the thermal energy is large enough to cause fluctuation in the local density, which allows the incoming molecules to disrupt the ordered striped phase. A coverage-induced phase transition then occurs, and the standing-up phase appears. In the case of α,ω-alkanedithiol, the measurements indicate that the local free energy minimum represented by the striped phase is very deep indeed.

While no denser phases were observed in the monolayers prepared by different growth methods, the quality of the striped phase was found to vary significantly. The monolayers that were grown by *in vacuo* gas-phase deposition at room temperature (Figure 2a) are of poorer quality as compared to those grown at elevated temperatures for which the domain size of the samples is substrate-limited as discussed in section III.B. These results can be tentatively attributed to the low diffusion rate of molecules at room temperature, which is expected from a system with a strong molecule−substrate interaction. This strong molecule−substrate interaction is also manifested by finding a similar domain size on the terraces and around surface heterogeneities (data not shown).

V. Thermal Properties

Apart from the structure and growth behavior, other monolayer properties such as thermal stability may be controlled by the interactions involved. GIXD was used to measure the thermal behavior of $HS-C_6-SH$ monolayers prepared using the "high-temperature growth" protocol. Figure 14a shows a selected set of azimuthal scans through the (0, 0.7) Bragg peak at different substrate temperatures. The radial resolution $\delta q_{||}$ was 0.02 $Å^{-1}$, and the striped phases IC1 and IC2 were not resolvable in this case. The integrated intensities measured are proportional to the total number of molecules that assemble either as IC1 or as IC2. Assuming a linear background and a Lorentzian peak shape, the integrated intensities were determined from the area under the peak of the azimuthal scans.

Figure 14b shows the evolution of the integrated intensities as a function of the substrate temperature. The data indicate that the integrated intensity remains basically unchanged up to 393 K while significant desorption takes place above 420 K. The integrated intensity drops to the noise level after annealing at ∼463 K for about 2 min. Instead of melting, desorption is believed to take place because no Bragg peak could be detected upon cooling of the substrate (data not shown). It might be that the melting temperature of the striped phases is close to or higher than the desorption temperature. Together with the structural findings discussed in section III.A, the changes of the peak width and the integrated intensity as a function of temperature can be rationalized as follows. The as-deposited monolayers are composed of two phases

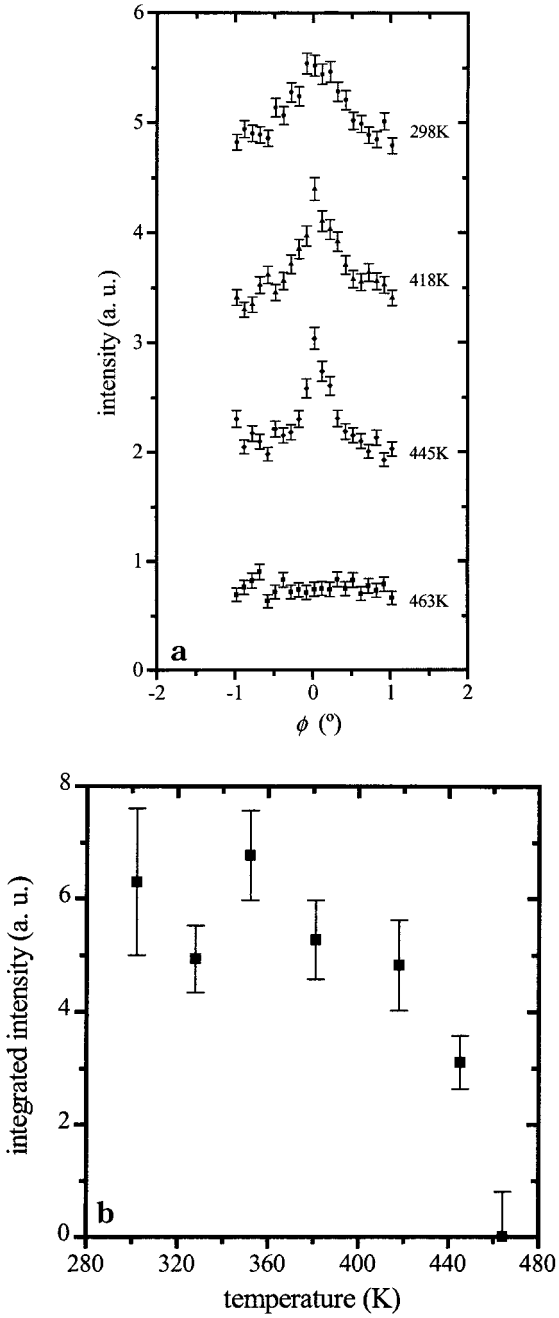

Figure 14. (a) Azimuthal scans through the (0, 0.7) peak at different substrate temperatures as indicated. All scans (except the one at 463 K) have been translated vertically by one arbitrary unit for viewing convenience. (b) The integrated intensities of the peaks under part a are plotted as a function of the substrate temperature for the striped phase of HS−C_6−SH.

IC1 and IC2. Upon annealing, the molecules diffuse, resulting in larger domains while the IC2 → IC1 phase transition takes place. Upon further annealing, IC1 desorbs from the substrate.

These results show that the striped phases of HS−C_6−SH are more thermally robust than the striped phase of HS−C_9−CH_3 which melts at ∼373 K[5] and then, as the dithiol, desorbs at ∼473 K.[29] Note that the boiling points of the bulk 1,6-hexanedithiol and *n*-decanethiol are almost the same.[30] The higher thermal stability of the HS−C_6−SH ordered phase is a consequence of the strong molecule−substrate interaction in the striped phases and is also consistent with the proposed model in which the molecular backbone is parallel to the surface, and for each molecule, there are two sulfur atoms interacting with the underlying substrate.

VI. Conclusions

The results of a multitechnique study of 1,6-hexanedithiol [$HS(CH_2)_6SH$] monolayers on Au(111) are presented. Three structural probes were employed: namely, STM, GIXD, and LEAD. Molecular resolution STM images of vapor-deposited monolayers show rows of bright features and suggest that the molecules lie prone on the surface and arrange in stripes. Two uniaxial incommensurate striped phases IC1 and IC2 were found by high-resolution GIXD. With respect to the surface substrate net, the diffraction patterns of both phases are consistent with a rectangular ($p \times \sqrt{3}$) net, where p is 4.24 in IC1 and 4.30 in IC2. The incommensurability is along the NN direction of the substrate, and the lattice spacing along this direction is 12.23 ± 0.04 Å for IC1 and 12.40 ± 0.02 Å for IC2. Within the experimental uncertainties, the lattice dimensions determined by GIXD and STM are in agreement. LEAD measurements are consistent with a rectangular net with unit mesh dimensions of 37.18 ± 0.65 Å × 4.995 ± 0.028 Å, which can be also described as a 3 × 1 superlattice with respect to the surface net observed by GIXD. Lattice nonuniformity along the NN direction of the substrate (in the direction of the chains) and angular broadening of the diffraction features were found by GIXD. From these measurements, it is suggested that the structure of the striped phases is comprised of fully extended molecules lying flat on the surface, with the plane containing the C atoms parallel to the surface. The incommensurability along the NN direction and the existence of the 3 × 1 superlattice imply the presence of multiple S/Au binding sites. In the proposed structure, the sulfur endgroups of adjacent molecules are separated by ∼2.9 Å and are parallel to the NN direction.

Different growth protocols, including the conventional liquid-phase deposition, have been attempted, but no evidence was obtained for the nucleation of ordered phases other than the striped phases described here. The apparent lack of crystalline high-density standing-up phases in HS−C_6−SH can be explained by a strong molecule−substrate interaction in the striped phases, which implies a large energy barrier for the diffusion of both the adsorbates and the domain boundaries. If other phases exist, the observations suggest that the striped phases are effective kinetic traps preventing the phase transition to other denser phases. Finally, the strong molecule−substrate interaction is manifested in the observed thermal behavior of the striped phases.

Recent results by Liu and collaborators[31] have shown that the growth of *n*-octadecanethiol monolayers can be made to proceed much faster and with better results by "nanografting" the molecules into a preexisting *n*-octadecanethiol monolayer using the tip of an atomic force microscope. It would therefore be interesting to nanograft dithiol molecules into an alkanethiol monolayer to see if in this way a standing-up monolayer can be obtained.

(29) Lavrich, D. J.; Wetterer, S. M.; Bernasek, S. L.; Scoles, G. *J. Phys. Chem. B* **1998**, *102*, 3456.

(30) The boiling point of 1,6-hexanedithiol is 391 K/15 mm from the *Aldrich Chemical Co. Catalog*. The boiling point of *n*-decanethiol is 399 K/19 mm from the *CRC Handbook of Physics and Chemistry*; Lide, D. R. Ed.; CRC Press: Boca Raton, FL, 1992.

(31) Xu, S.; Laibinis, P. E.; Liu, G.-Y. *J. Am. Chem. Soc.* **1998**, *120*, 9356.

The present study highlights the importance of understanding the relationship between the energetics, structure, and growth of thiol monolayers on gold. Also, the results obtained for hexanedithiol on gold show once more the importance of the striped phase in the growth process of these films.[5,6,23] The present study demonstrates that a combination of STM, GIXD, and LEAD may be necessary to obtain reliable structural information at a molecular level, without which the utilization of these molecules in the assembly or fabrication of nanomaterials and/or nanodevices may be complicated by the possibly false underlying premises.

Acknowledgment. We acknowledge Dr. P. Fenter for illuminating discussions. Thanks are due to Dr. P. Schwartz for his technical support in the LEAD measurements. F. Schreiber acknowledges the financial support from the DFG. The GIXD studies are supported by Department of Energy under Grant DE-FG02-93ER45503. The GIXD measurements were carried out at the National Synchrotron Light Source which is supported by Department of Energy Contract DE-AC0276CH-00016.

LA9906222